PNAS
www.pnas.org

Supplementary Information for

Magnetoelastic hybrid excitations in non-centrosymmetric $CeAuAl_3$

P. Čermák, A. Schneidewind, B. Liu, M. M. Koza, C. Franz, R. Schönmann, O. Sobolev, C. Pfleiderer

Corresponding Authors:
Petr Čermák, E-mail: cermak@mag.mff.cuni.cz,
Christian Pfleiderer, E-mail: christian.pfleiderer@tum.de

This PDF file includes:

Supporting Information Text

Experimental details

The neutron scattering measurements were carried out on the triple-axis spectrometers PUMA and PANDA at MLZ (1, 2). The experimental setups involved double-focussing PG002 monochromators and analyzers and a closed-cycle cryostat for sample cooling. In the measurements at PUMA, data were recorded in the (h, 0, l) and (h, k, 0) plane using constant $k_\mathrm{f} = 2.662$ Å^{-1} and two PG-filters after the sample. To determine the resolution, selected scans were recorded at the PG004 reflection of the analyzer. At PANDA, high-resolution measurements were carried out in (h, 0, l) orientation of the sample using $k_\mathrm{f} = 1.57$ Å^{-1} with cooled Be-filter. Further data were recorded using $k_\mathrm{f} = 1.97$ Å^{-1} with a PG-filter after the sample. The positions in q-space where spectra were collected are shown in Fig. S1.

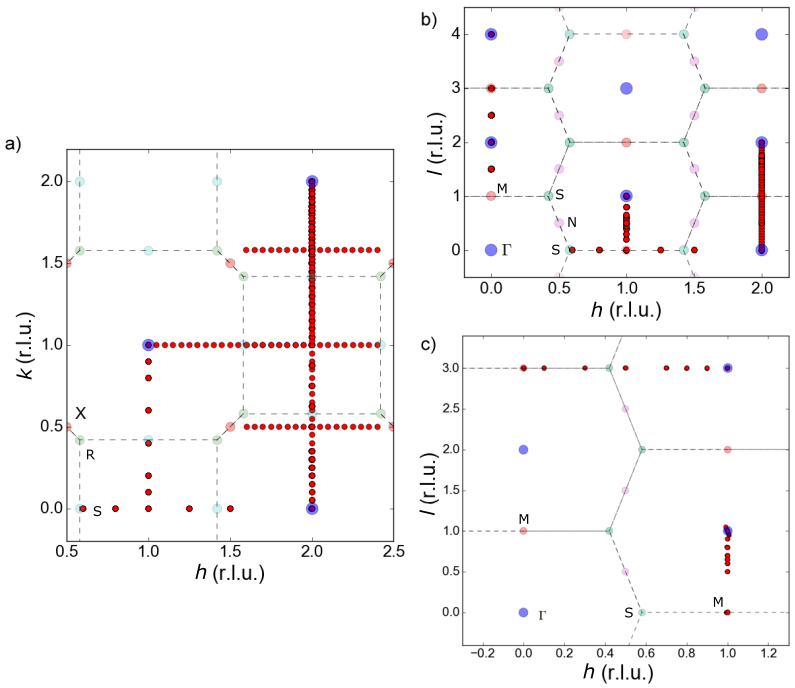

Fig. S1. Location of all data points measured on PUMA in the (h, 0, l) sample orientation (panel (a)), and the (h, k, 0) sample orientation (panel (b)). (c) Projection of the location of all data points measured at PANDA.

Crystal field analysis

The pure crystal field levels without taking into account perturbations were analyzed using the standard Stevens formalism (3). The position of the Ce atoms in $CeAuAl_3$ is characterized by the point group symmetry C_{4v} (*4mm* in int. notation). This allows to reduce the general crystal field Hamiltonian to:

$$H^0_{CEF} = B^0_2 O^0_2 + B^0_4 O^0_4 + B^4_4 O^4_4, \qquad [1]$$

where B^m_n and O^m_n are the CEF parameters and Steven's operators, respectively (3, 4). In the paramagnetic phase the sixfold degenerate Ce^{3+} state ($J = \frac{5}{2}$), which corresponds to a $4f^1$ configuration, is split into three doublets:

$$\begin{aligned} |\Gamma_6\rangle &= |\pm\frac{1}{2}\rangle \\ |\Gamma_7^{(1)}\rangle &= \alpha|\pm\frac{5}{2}\rangle - \beta|\mp\frac{3}{2}\rangle \\ |\Gamma_7^{(2)}\rangle &= \beta|\pm\frac{5}{2}\rangle + \alpha|\mp\frac{3}{2}\rangle \end{aligned} \qquad [2]$$

Neutron scattering of the crystal field transitions between these states on a single crystal sample bears the advantage, that different ground states may be distinguished directly from a comparison of the different crystallographic directions. The intensity of the transition between two CF levels depends on the matrix elements of the transition matrix

$$S(\boldsymbol{Q}, E)_{E_n \to E_m} = c \cdot \big(f(\boldsymbol{Q})\big)^2 P_n \sum_\alpha |\langle\Gamma_m|J^\alpha|\Gamma_n\rangle|^2 \delta(E - E_n - E_m), \qquad [3]$$

where $f(\boldsymbol{Q})$ is the magnetic form factor, P_n expresses thermal occupation of level E_n, $\alpha = x$, y or z, and $\boldsymbol{J}$ is the total angular momentum operator. Since neutrons are sensitive to the magnetic moment perpendicular to $\boldsymbol{Q}$ only, it is possible to observe the different J^α matrices.

Because of the simple form of the J^z matrix, it does not contribute to transitions from/to the $|\Gamma_6\rangle$ state. Consequently, for the case of the $|\Gamma_6\rangle$ ground state, the J^x and J^y components may be measured together along the crystallographic c direction whereas only J^x, J^y is measured along the b, a direction, respectively. In addition, transition intensities along the a- and b-axis are the same in the tetragonal structure. On the other hand, for the $|\Gamma_7^{(1)}\rangle$ or $|\Gamma_7^{(2)}\rangle$ ground states the J^z component will always contribute to the transition from and to the ground state.

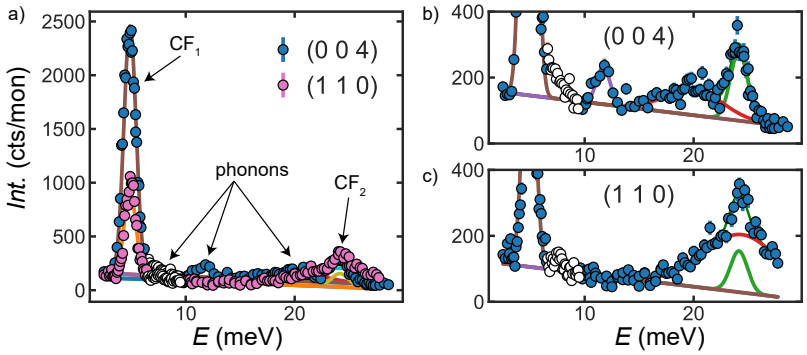

Fig. S2. (a) Energy scans in two different crystallographic directions. The monitoring rate of the data was corrected for higher order contamination. Arrows indicate the observed crystal field levels as well as contamination by phonons. Data marked by white symbols were not taken into account in the analysis as the contamination due to phonons was difficult to fit. (b) and (c) Close-up view of the data. The lines represent Gaussians.

Energy scans were recorded at $Q = (0, 0, 4)$ and $Q = (1, 1, 0)$ between 2 and 28 meV on the spectrometer PUMA. An analytic correction of the monitor for higher order scattering was applied to the raw data. Both spectra are shown in Fig. S2(a). The intensities of the peaks inferred from fits of the data are summarized in table S1. As stated above, for the case of the $|\Gamma_6\rangle$ ground state we find $I_{(004)} \approx 2 \cdot I_{(110)}$, otherwise $I_{(004)} < 2 \cdot I_{(110)}$. Thus, the ground state is in excellent agreement with $|\Gamma_6\rangle$, consistent with Ref. (5).

For the detailed determination of the crystal field parameters, Monte-Carlo calculations were used to visualize the possible solutions in a depiction of B_2^0, B_4^0 and B_4^4 shown in Fig. S3. This analysis underscores, that for given ratio of the CF excitation to the ground state, there exist only two independent solutions (and another two with opposite sign of B_4^4 parameter which is indistinguishable using neutron scattering). Two of these four solutions are in agreement with the $|\Gamma_6\rangle$ ground state. A Generalized Reduced Gradient (GRG2) (6) nonlinear optimization algorithm was used to refine the detailed B parameters, resulting in $B_2^0 = 1.203, B_4^0 = -0.00095$ and $B_4^4 = \pm 0.244$ meV. The parameters accounting for the crystal field splitting calculated from this set of B values are denoted in Table S1.

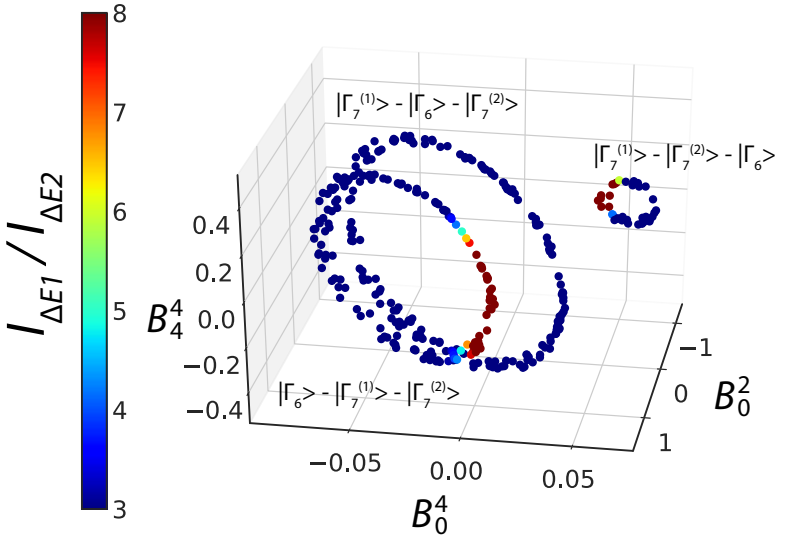

Fig. S3. Visualization of the possible crystal field parameters resulting in an energy splitting of $\Delta_1 = 4.885\text{meV} \pm 5\%$ and $\Delta_2 = 24.16\text{meV} \pm 5\%$. Different rings represent a different order of CEF states. The color coding serves to highlight the ratio between the intensities of two crystal field peaks.

Table S1. Intensities of the CF transitions

	measured					calculated		
Q	I_{CF1}	I_{CF2}	I_{CF1}/I_{CF2}	E_1	E_2	I_{CF1}/I_{CF2}	E_1	E_2
(0, 0, 4)	3220(50)	420(80)						
(1, 1, 0)	1140(30)	250(70)		4.885(7)	24.16(9)	6.6	4.949	24.26
averaged J_x	1450(30)	220(50)	6.6(1.7)					

Becker-Fulde-Keller theory

Pure CEF excitations are expected to have negligible lifetime. In turn, the width of the CEF peaks is expected to be limited by the resolution of the spectrometer and temperature independent. As shown in Fig. S4(a) this is not the case for $CeAuAl_3$. Data shown here were simultaneously fitted at seven different temperatures using the same constant background and same width of the peaks. An alternative analysis is reported in the main text, where the same data were fitted with an independent sloping background and an independent width of the peaks (cf. Fig. 3(a) in the manuscript). While the quality of the fits is very good, the temperature dependence of the intensities inferred from the fits does not follow the expected behaviour as shown in Fig. 3(b) in the main text.

The reason is that part of the magnetic intensity transfers into the background with increasing temperature. This effect is well described by a theoretical model proposed by by Becker, Fulde and Keller (BFK) (7). In order to compare the experimental data with the predictions of BFK theory, the original code written by Keller was used, available as an open source of the McPhase suite (8). Unfortunately, the original code in FORTRAN is very slow and not suitable for fitting. The code was therefore enhanced and recompiled with a PYTHON interface and published as a part of CrysFiPy software (9). The results of the fit are shown in Fig. S4(b), where all seven energy scans were fitted simultaneously with the BFK model (using a single FWHM and a flat background) and a coupling constant $g_{\mathrm{BFK}} = 0.022$ was obtained. Note, that the BFK model corresponds to second order perturbation theory with respect to coupling constant g_{BFK}. Therefore, the BFK model is inaccurate at the lowest temperatures, since it does not account for the broadening of $|\Gamma_6\rangle$ into a heavy band by the Kondo lattice effect. Yet, these effects are negligible and do not change our analysis.

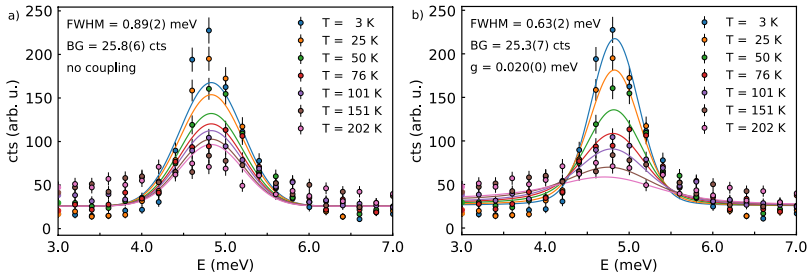

Fig. S4. Energy scans at Q = (0, 0, 3) at different temperatures (see als legend for details). a) Data were fitted with a Gaussian of the same width and fixed intensity ratios regarding population of pure CF excitation from the ground state. b) Data were fitted with Becker-Fulde-Keller theory. Resulting fit parameters are stated in the figure.

Analysis of the anti-crossing

In order to account for the anti-crossing and to evaluate the coupling energy, the results of Aksenov and coworkers for $PrAl_2$ (10) and later $PrNi_5$ (11) were adapted. A detailed procedure may be found in Ref. (12), which addresses coupled excitations in paramagnetic regime. In the following the main steps of the calculations are summarized. A double-time Green function method was used to describe the coupling of the lattice to magnetic ions for cubic symmetry and zero field. While in $PrNi_5$ the anti-crossing due to the dipole transition $\Gamma_4 - \Gamma_5$ is observed by neutron scattering, in case of $PrAl_2$ the quadrupolar transition $\Gamma_3 - \Gamma_4$ would not be neutron active without coupling to the lattice.

For $CeAuAl_3$, the calculation needs to be extended to tetragonal symmetry. To do so the f-electrons are treated as strictly localized, because the first CEF excitation at E=59.2 K (13) lies well above T_{K} (14). For a standard Hamiltonian of RE metallic compounds, taking the magneto-elastic interaction into account, the one-phonon Green-function (GF) in the random phase approximation may be expressed as (10, 11)

$$D(\boldsymbol{q},\omega) = \left[\left(D^0(\boldsymbol{q},\omega)\right)^{-1} - \sum_{mn} G_{mn}(\boldsymbol{q},\omega)\right]^{-1}, \qquad [4]$$

where $D^0(\boldsymbol{q},\omega)$ is the phonon GF in the harmonic approximation, $\boldsymbol{q}$ is wave vector of phonons, and

$$G_{mn}(\boldsymbol{q},\omega) = \frac{E_{mn} V^1_{mn} V^1_{nm} (f_m - f_n)^2}{\omega^2 - E^2_{mn}}, \qquad [5]$$

where $f_m = \exp(-\beta E_m)/\sum_m \exp(-\beta E_m)$ is the occupation number of one-ion states, and E_{mn} are energies of transitions between CEF levels. $V^1_{mn} = \langle m|V_1(\boldsymbol{J},\boldsymbol{q})|n\rangle$ are matrix elements of the operators $V_1(\boldsymbol{J},\boldsymbol{q})$ which are functions of the $\boldsymbol{J}$ operators depending on the symmetry of the magneto-elastic coupling (15).

The total Hamiltonian of the system may be written as

$$H^f_{CEF} = H^0_{CEF} + H^I_{me}, \quad [6]$$

H^f_{CEF} denotes the interaction of the spin $\boldsymbol{J}$ of the f-th ion with the crystal field caused by the other ions, with the zeroth-order term H^0_{CEF} being the conventional crystal field Hamiltoninan described by Eq. (1) and also solved there. H^I_{me} is the one-ion magneto-elastic interaction, coupling the spin system to the strain. At low temperature, only the lowest-lying level is occupied. In the following the low-energy transition $|\Gamma_6\rangle \rightarrow |\Gamma^1_7\rangle$ at $E_{\Gamma_6\Gamma^1_7} = 4.9\,\mathrm{meV}$ is considered, which crosses the acoustic phonon.

The one-ion magneto-elastic Hamiltonian accounts for the direct coupling between the deformations of the lattice and the $4f$ shell. This Hamiltonian may be constructed according to group theory (16). Let $\mathcal{S}^{\Gamma,j}_i (i = 1, 2, \cdots, n)$ be the spin functions which form a basis for the n-dimensional representation Γ, different sets being distinguished by j =1, 2. Then the one-ion contributions H^I_{me} to the magneto-elastic Hamiltonian may be written as

$$H^I_{me} = -\sum_{\Gamma}\sum_{j,j'} \widetilde{B}^{\Gamma}_{jj'}(f) \sum_i \epsilon^{\Gamma,j}_i \mathcal{S}^{\Gamma,j'}_i(f), \quad [7]$$

where $\widetilde{B}^{\Gamma}_{jj'}$ is a phenomenological magneto-elastic coupling constant, and $\epsilon^{\Gamma,j}_i$ represents linear combinations of the first-order strain components ϵ_{xx}, ϵ_{yy}, ϵ_{zz}, ϵ_{xy}, ϵ_{yz}, and ϵ_{zx}. The shear strains are defined as $\epsilon_{xy} = \frac{1}{2}(\frac{\partial u_y}{\partial x} + \frac{\partial u_x}{\partial y})$.

It is reasonable to assume that the crystal is constrained so that all "antisymmetric strains" such as $\frac{1}{2}(\frac{\partial u_y}{\partial x} - \frac{\partial u_x}{\partial y})$, which correspond to homogeneous rotations of the crystal, vanish. Whereas in zero applied magnetic field the rotational magneto-elastic interaction may be expected to contribute to the phonon dispersion curves for finite $\boldsymbol{q}$-values (17), the coupling is expected to give corrections of a few percent only. Therefore, these terms will not be considered in this work. $\mathcal{S}^{\Gamma,j'}(f)$ corresponds to the spin operators of the ion at site f, as shown in Table S2. As Eq. (7) has been derived assuming homogeneous strains, it is only valid for long-wavelength acoustic phonons (18).

Table S2. Strain functions and one-ion spin operators for the tetragonal system.

Strain functions $\epsilon^{\Gamma,j}_i$	One-ion operators $\mathcal{S}^{\Gamma,j'}(f)$
$\epsilon^{\alpha 1} \equiv \frac{\sqrt{3}}{3}(\epsilon_{xx} + \epsilon_{yy} + \epsilon_{zz})$	1
$\epsilon^{\alpha 2} = \sqrt{\frac{2}{3}}[\epsilon_{zz} - \frac{1}{2}(\epsilon_{xx} + \epsilon_{yy})]$	$3J_z^2 - J(J+1)$
$\epsilon^{\gamma} = \frac{\sqrt{2}}{2}[\epsilon_{xx} - \epsilon_{yy}]$	$J_x^2 - J_y^2 = \frac{1}{2}(J_+^2 + J_-^2)$
$\epsilon^{\delta} = \sqrt{2}\epsilon_{xy}$	$P_{xy} = \frac{1}{2}(J_xJ_y + J_yJ_x)$
$\epsilon^{\epsilon}_1 = \sqrt{2}\epsilon_{yz}$	$P_{yz} = \frac{1}{2}(J_yJ_z + J_zJ_y)$
$\epsilon^{\epsilon}_2 = \sqrt{2}\epsilon_{zx}$	$P_{zx} = \frac{1}{2}(J_xJ_z + J_zJ_x)$

Thus the one-ion magneto-elastic Hamiltonian for the tetragonal symmetry (point group $4mm$) may be expressed directly as (19)

$$\begin{aligned} H^I_{me}(f) = &- \widetilde{B}^{\alpha_1}\epsilon^{\alpha 1}\left[3J_z^2 - J(J+1)\right] \\ &- \widetilde{B}^{\alpha_2}\epsilon^{\alpha 2}\left[3J_z^2 - J(J+1)\right] \\ &- \widetilde{B}^{\gamma}\frac{\sqrt{2}}{2}(\epsilon_{xx} - \epsilon_{yy})(J_x^2 - J_y^2) \\ &- \widetilde{B}^{\delta}\frac{\sqrt{2}}{2}\epsilon_{xy}(J_xJ_y + J_yJ_x) \\ &- \widetilde{B}^{\epsilon}\frac{\sqrt{2}}{2}\epsilon_{yz}(J_yJ_z + J_zJ_y) \\ &- \widetilde{B}^{\epsilon}\frac{\sqrt{2}}{2}\epsilon_{xz}(J_xJ_z + J_zJ_x), \end{aligned} \quad [8]$$

In other words, the magneto-elastic Hamiltonian may be considered as the strain derivative of the crystal field Hamiltonian. The two-ion magneto-elasticity is in turn related to the modification of the two-ion magnetic interactions by the strain. The last three terms describe a quadrupolar interaction. However, it is important to emphasize that we do not consider the presence of multipolar order nor the coupling of the excitations of multipolar order to the phonons.

The one-ion magneto-elastic Hamiltonian is sufficiently general when considering the main effects. Therefore, in this study two-ion magneto-elastic interactions were ignored which may lead to structural and magnetic phase transitions (15). In addition, the experimental data (even under an applied magnetic field) was analysed in terms of $V_1(\boldsymbol{J},\boldsymbol{q})$, i.e., neglecting the second order magneto-elastic interaction as well as the linear rotational interaction.

We specialize our example of magneto-elastic interaction of shear deformations within the $x-z$ plane (all $\frac{\partial u_\alpha}{\partial \beta}=0$ except $\frac{\partial u_x}{\partial z}$ and $\frac{\partial u_z}{\partial x}$). Then we have

$$V_1(\boldsymbol{J},\boldsymbol{q}) \sim e_z(q_x)q_x(J_xJ_z+J_zJ_x), \quad [9]$$

where $\boldsymbol{e}(\boldsymbol{q})$ is the polarization vector for the phonon.

For the $\Gamma-$M direction, only the matrix elements determined by $\Gamma_6^A-\Gamma_7^{1B}$ and $\Gamma_6^B-\Gamma_7^{1A}$ differ from zero. Using the wave functions of one-ion states, the matrix elements for Eq. (5) may be obtained in the form

$$|V^1_{\Gamma_6^A\Gamma_7^{1B}}| = |V^1_{\Gamma_6^B\Gamma_7^{1A}}| = 2\sqrt{2}\alpha\widetilde{B}^\epsilon|\boldsymbol{q}|, \quad [10]$$

where $\widetilde{B}^\epsilon$ is the magneto-elastic coupling constant and $|\boldsymbol{q}|$ is reciprocal wavevector. In order to compare the coupling in different materials, we introduce an effective coupling constant $g_{\rm AC}$, which is directly related to the renormalization of elastic constant (see Eq. 37 in Ref. (18) with $g_{\rm AC}=\widetilde{g}^2$):

$$g_{\rm AC} = \frac{(\widetilde{B}^\epsilon)^2}{c_{44}\Omega} = \frac{(\widetilde{B}^\epsilon)^2}{v_s^2 m_c} = \frac{\hbar^2(\widetilde{B}^\epsilon)^2q^2}{\omega_0^2 m_c}, \quad [11]$$

where c_{44} is an elastic constant, Ω is the volume of the primitive cell, v_s is the speed of sound and m_c is the mass of the primitive cell. Using Eqs. (4) and (5), the coupled quadrupole-phonon dispersion $\omega(\boldsymbol{q})$ may be determined by the poles of the Green-Function (4), i.e., by setting the denominator of Eq. (5) equal to zero (15):

$$(\omega_{\mathbf{q}}^2)^2 - \omega_{\mathbf{q}}^2E^2_{\Gamma_6\Gamma_7^1} - \omega_0^2\omega_{\mathbf{q}}^2 + \omega_0^2E^2_{\Gamma_6\Gamma_7^1} - \frac{\hbar^2}{m_c}E_{\Gamma_6\Gamma_7^1}(|V_{\Gamma_6^A\Gamma_7^{1B}}|^2+|V_{\Gamma_6^B\Gamma_7^{1A}}|^2) = 0. \quad [12]$$

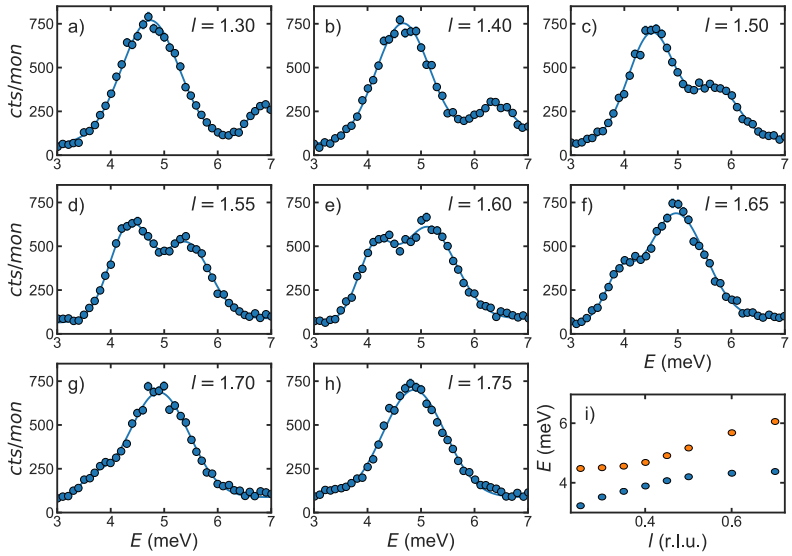

Fig. S5. (a-h) Energy scans recorded at the PUMA spectrometer at positions (20l). Data are fitted with two Gaussians and the same sloping background. (i) Dispersion relations inferred from the maximum of the fits.

One may finally obtain the mixed mode dispersion as:

$$\omega^2_{\mathbf{q}\pm} = \frac{E^2_{\Gamma_6\Gamma_7^1}+\omega_0^2}{2} \mp \left[\left(\frac{E^2_{\Gamma_6\Gamma_7^1}-\omega_0^2}{2}\right)^2 + 16\alpha^2E_{\Gamma_6\Gamma_7^1}\omega_0^2g_{\rm AC}\right]^{\frac{1}{2}}, \quad [13]$$

With equation (13), the magneto-elastic constant may be inferred from the experimental data. For the modelling of the acoustic phonon dispersion, the simplest possible model was used corresponding to a 1D chain:

$$\omega_q = A\sqrt{1-\cos(|\boldsymbol{q}|)} \quad [14]$$

where A is related to the amplitude of the branch at the border of the Brillouin zone. At first data points were determined by Gaussian fits of the raw data, Fig. S5(a-h). This approach ignores intensities of the excitations and results in the set of data points shown in Fig. S5(i). The data were subsequently fitted with the model described by Eq. (13) and (14). The results of the fit are shown in Fig. S6 with all points measured also in different Brillouin zones (see Fig. 2 in the manuscript for color coding). The results of the fit may be summarized as follows: $A = 5.439(6)$ meV, $E_{\Gamma_6\Gamma_7^1} = 4.952(3)$ meV and $g_{\rm AC} = 12.1(2)\,\mu$eV.

In order to compare our effective coupling constant with the results of Aksenov on $PrNi_5$ (11), we refitted their data. In particular, it appears that the dependence of the matrix elements V_{mn} on the wavevector q and a factor of 1/2 were not taken

into account. The expression we used instead to account for the coupled CEF-phonon excitation mediated by quadrupolar interactions in $PrNi_5$ may be expressed as:

$$\omega^2_{\mathbf{q}\pm} = \frac{E^2_{\Gamma_4\Gamma_{5A}} + \omega_0^2}{2} \mp \left[\left(\frac{E^2_{\Gamma_4\Gamma_{5A}} - \omega_0^2}{2}\right)^2 + \frac{9.82^2}{2} E_{\Gamma_4\Gamma_{5A}} \omega_0^2 g_{\mathrm{AC}}\right]^{\frac{1}{2}}, \quad [15]$$

Refitting the data reported n $PrNi_5$ we obtain as an upper bound $g_{\mathrm{AC}} < 4\,\mu$eV, which is much smaller than for $CeAuAl_3$. An exact determination of the coupling constant is unfortunately due to resolution of the data as illustrated in Fig. S6 (b).

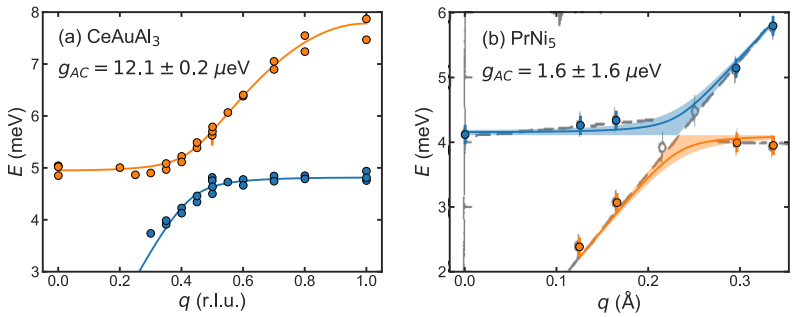

Fig. S6. (a) Anti-crossing of the TA phonon branch and the crystal field excitation in $CeAuAl_3$. The solid lines are the result of the fit of the Eq. (13) to the measured data. (b) Anti-crossing in $PrNi_5$. Solid lines are result of the fit of the Eq. (15) to the data measured by Aksenov (11). Due to the lack of resolution, two nearest points to the crossing point were excluded from the fitting procedure, as there is not possible to distiguish peak splitting. The shaded area denotes possible solutions with a respect to the fitted error. Black underlying data in the background were taken from Ref. (11). On the basis of this fit we estimate the effective anti-crossing coupling constant in $PrNi_5$ to be smaller than 4 μeV.

Vibronic bound state

The total Hamiltonian may be written as

$$H_{total} = H_{CEF} + \hbar\omega_0(a_u^+ a_u + 1/2) - g(a_u + a_u^+)O_u, \quad [16]$$

where the first term is the tetragonal CEF Hamiltonian mentioned above, the second term is the phonon Hamiltonian (H_{ph}), and the third term is the c-ph coupling term. Here $\hbar\omega_0$ denotes the phonon energy, and $a_{\boldsymbol{u}}^+$ or $a_{\boldsymbol{u}}$ are phonon creation or annihilation operators, $\boldsymbol{u}$ is the phonon displacement, and g is a magneto-elastic parameter proportional to the coupling between CEF and phonon excitations. O_u is the CEF-phonon operator, with $u = \alpha, \gamma, \delta, \epsilon_1$ and ϵ_2. According to ref.(13), the CEF-phonon operator should be of the form

$$O_\gamma = O_2^2 = J_x^2 - J_y^2 = \frac{1}{2}(J_+^2 + J_-^2). \quad [17]$$

In the basis states of the CEF states, O_γ is given by

$$O_\gamma = \begin{pmatrix} 0 & 0 & O_\gamma^{13} & 0 & 0 & O_\gamma^{16} \\ 0 & 0 & 0 & O_\gamma^{13} & O_\gamma^{16} & 0 \\ O_\gamma^{13} & 0 & 0 & 0 & 0 & 0 \\ 0 & O_\gamma^{13} & 0 & 0 & 0 & 0 \\ 0 & O_\gamma^{16} & 0 & 0 & 0 & 0 \\ O_\gamma^{16} & 0 & 0 & 0 & 0 & 0 \end{pmatrix}, \quad [18]$$

with

$$O_\gamma^{13} \equiv \langle 1|O_\gamma|3\rangle = -3\sqrt{2}\alpha + \sqrt{10}\beta, \quad [19]$$

$$O_\gamma^{16} \equiv \langle 1|O_\gamma|6\rangle = \sqrt{10}\alpha + 3\sqrt{2}\beta. \quad [20]$$

Then the oscillator strengths Q_γ is given by

$$Q_\gamma = \begin{pmatrix} 0 & 15.0928 & 40.9046 \\ 15.0928 & 0 & 0 \\ 40.9046 & 0 & 0 \end{pmatrix} \quad [21]$$

with $Q_{\alpha\beta} = \sum_{nm} |\langle \Gamma_\alpha^m | O_\gamma | \Gamma_\beta^n \rangle|^2$. We have $Q_\gamma^{\Gamma_6\Gamma_7^2} = Q_\gamma^{\Gamma_7^2\Gamma_6} = 40.9046$ and $Q_\gamma^{\Gamma_6\Gamma_7^1} = Q_\gamma^{\Gamma_7^1\Gamma_6} = 15.0928$. This shows that the phonon coupling is possible only to the inelastic $\Gamma_6 \leftrightarrow \Gamma_7^1$ and $\Gamma_6 \leftrightarrow \Gamma_7^2$ transitions.

The eigenstates of H_{total} are calculated within the eight-dimensional subspace $|\psi_k\rangle, k = 1, 2, \cdots, 8$ of zero- and one-phonon states $|\Gamma_6, 0\rangle$, $|\Gamma_7^1, 0\rangle$, $|\Gamma_7^2, 0\rangle$ and $|\Gamma_6, 1\rangle = a^+|\Gamma_6, 0\rangle$ with unperturbed energies 0, $E_{\Gamma_6\Gamma_7^1}$, $E_{\Gamma_6\Gamma_7^2}$, and $\hbar\omega_0$, respectively. The

diagonalization of the Hamiltonian H_{total} yields phonon-like states, which represent linear combinations of purely electronic $|\Gamma_7^2, 0\rangle$ states and one-phonon states $|\Gamma_6, 1\rangle$:

$$|\widetilde{\Gamma_7^2}\rangle = e|\Gamma_6, 1\rangle + \sqrt{1-e^2}|\Gamma_7^2\rangle, \qquad [22]$$

This may be interpreted as bound states of a CEF excitation with phonons.

For a rough estimate of the coupling constant g_{VBS} we have assumed $\hbar\omega_0 = 6.5$ meV, just between E_{CF} and E_{VBS}. This value is in agreement with an enhanced density of phonon states as determined in DFT calculations (see Fig. 2 in the manuscript). In the next step, the CEF Hamiltonian leading to unperturbed CEF transitions at $E_{\mathrm{CF1}} \approx \hbar\omega_0$ and $E_{\mathrm{CF2}} = 24.2$ meV was guessed. In turn, the coupling constant was fitted to the measured energy transitions at E_{CF1}, E_{VBS} and E_{CF2} resulting in $g_{\mathrm{VBS}} \approx 400\,\mu$eV. This approximation is based on a simple model assuming non-dispersive phonon states. For the correct treatment of the vibronic coupling in $CeCuAl_3$ one needs to involve a more complex theoretical apparatus.

We will now discuss the relation between coupling constants of the VBS and the anti-crossing, g_{VBS} and g_{AC}, respectively. The constants appear to differ by an order of magnitude. However, their values are not directly related for the following reasons:

(a) For g_{VBS}, we adopted Adroja's treatment (13) and in the Hamiltonian we used also the operator $O_2^2 = J_x^2 - J_y^2$ for the magneto-elastic term. But for g_{AC}, we used another operator, namely $J_xJ_z + J_zJ_x$, accounting for shear deformations. The former operator does not lead to the appearance of mixed modes for transverse phonons with $q \cdot e = 0$. Further, different operator will lead to different matrix elements, such that the pre-factors of g_{AC} and g_{VBS} can be compared.

(b) For the vibronic bound state a simplified model was used, where the phonon is dispersionless and the phonon energy is constant. For the anti-crossing the phonons are q-dependent. These two methods are different. The former is directly diagonalizing the total Hamiltonian, while the latter requires use of a phonon Green-function. This should produce only a small difference in g-values.

(c) The final value of g_{AC} obtained by fitting the INS data represents an *effective coupling constant*. It is obtained from the *phenomenological magneto-elastic coupling constant* $\widetilde{B}^{\Gamma}_{jj'}$ and material constants of the sample using Eq. (11). On the other hand, g_{VBS} directly indicates the strength of the mixing between CEF levels and phonons. It does not scale with the magneto-elastic coupling constants.

Additional figures and resources

In the following additional figures are presented to illustrate further the phenomena described in the main text. Fig. S7 shows the momentum dependence of the crystal field and vibronic excitations, which decreases with increasing momentum following closely the form factor of the Ce^{3+} ion (solid line).

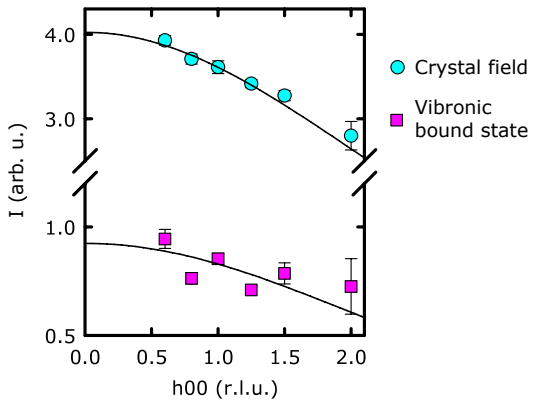

Fig. S7. Q-dependence of the integrated intensities of the crystal field and vibronic bound state along the (h, 0, 0) direction. The black line denotes a fit to the form factor of the Ce^{3+} ion. The data at the last point, (2, 0, 0), were measured for a different sample orientation and with lower statistics, accounting for the larger error bars.

The anti-crossing described in the main text was observed for different positions in Q-space. The effect was not always evident due to the tilt of resolution elipsoid. In order to illustrate this, data across the anti-crossing are shown for three different Brillouin zones in Fig. S8. Fig. S8(a) was also shown in the main text. It displays the anti-crossing nearby a weak reflection (101), notice enhanced intensity of the CF mode between anti-crossing and middle of the Brillouin zone 101. This effect may be caused by an underlying softened optical phonon and agrees with the single oscillator model for the VBS since the $|\Gamma_6\rangle$ -> $|\Gamma_7^1\rangle$ transition and the phonon frequency around Gamma become progressively detuned suppressing the VBS intensity. Polarized neutron scattering experiments will be needed to resolve this issue. Further, Fig. S8(b) shows the anti-crossing nearby the strong elastic reflection at (202). Here the CEF intensity is constant on both sides of the anti-crossing and the phonon branch across the anti-crossing is enhanced. The anti-crossing effect is, finally, barely visible nearby the (114) Γ-point due to the instrumental resolution as shown in Fig. S8(c).

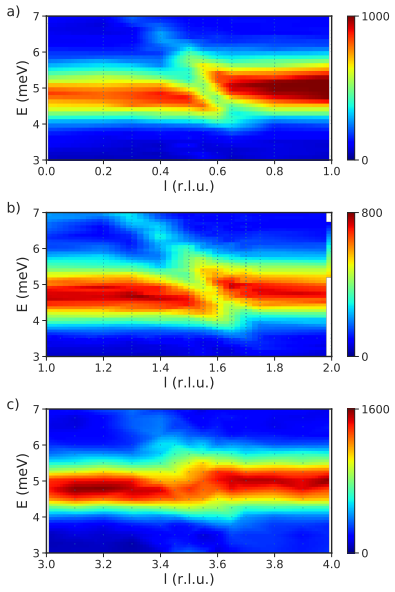

Fig. S8. Intensity maps measured on PUMA instrument in the a) 10L, b) 20L and c) 11L region.

Detailed energy scans through different Q-points of the anti-crossing in the (101) Brillouin zone is shown in Fig. S9(a) and its temperature dependence is in Fig. S9(b). The enhanced intensity in the middle of the Brillouin zone (Γ-point, red area) as compared to the M-point (green area) was already discussed in the main text. This effect is not visible for the (202) Γ-point, cf. Fig. S9(c).

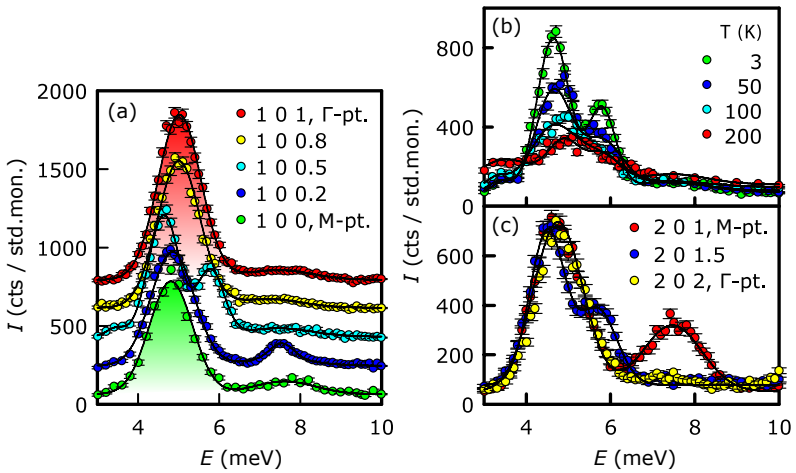

Fig. S9. Constant Q scans normalized to the standard monitor. Black lines are results of the fit of Gaussians. (a) Comparison of the width and intensities of the anti-crossing in the (101) Brillouin zone. Note the unusual enhancement of the CF intensity which decreases with lower Q (from red to green). Data are shifted vertically by 200 cts for clarity. (b) Temperature dependence of the anti-crossing between phonon and crystal field at the (1 0 0.5) point. See that the whole intensity scales down as expected from the crystal field level. Lines are Gaussian fits to the data. (c) Comparison of the width and intensities of the anti-crossing in the (202) Brillouin zone.

References

1. A. Schneidewind and P. Čermák. PANDA: Cold three axes spectrometer. *JLSRF*, 1:12, 2015.
2. O. Sobolev and J. T. Park. PUMA: Thermal three axes spectrometer. *JLSRF*, 1:13, 2015.
3. M.T. Hutchings. Pt.-charge calc. of energy lev. of magn. ions in CEFs. In F. Seitz and D. Turnbull, editors, *Sol. St. Phys.*, volume 16, page 227. Acad. Press, 1964.
4. E. Balcar and S.W. Lovesey. *Theory of Magnetic Neutron and Photon Scattering*. Oxford Ser. Neutr. Scatt. Cond. Matt. Clarendon Press, 1989. ISBN 9780191589119.
5. D. T. Adroja, C. de la Fuente, A. Fraile, A. D. Hillier, A. Daoud-Aladine, W. Kockelmann, J. W. Taylor, M. M. Koza, E. Burzurí, F. Luis, J. I. Arnaudas, and A. del Moral. musr and neutron scatt. study of the noncentrosymm. tetrag. comp. $CeAuAl_3$. *Phys. Rev. B*, 91:134425, 2015.
6. L. S. Lasdon, A. D. Waren, A. Jain, and M. Ratner. Design and testing of a generalized reduced gradient code for nonlinear programming. *ACM Trans. Math. Softw.*, 4:34–50, 1978.
7. K. W. Becker, P. Fulde, and J. Keller. Line width of crystal-field excitations in metallic rare-earth systems. *Z. Phys. B*, 28:9–18, 1977.
8. M Rotter. Using McPhase to calculate magnetic phase diagrams of rare earth compounds. *J. Mag. Mag. Mat.*, 272-276: E481 – E482, 2004.
9. P. Cermak, B. Liu, J. Zubac, and K. Pajskr. Crysfipy. https://crysfipy.readthedocs.io/, 2017–2018.
10. V. L. Aksenov, Th. Frauenheim, N. M. Plakida, and J. Schreiber. Magneto-vibrational excitations in $PrAl_2$. *J. Phys. F*, 11:905, 1981.
11. V.L. Aksenov, E.A. Goremychkin, E. Mühle, Th. Frauenheim, and W. Bührer. Coupled quadrupole-phonon excitations: Inelastic neutron scattering on van vleck paramagnet $PrNi_5$. *Physica B+C*, 120:310 – 313, 1983.
12. B.-Q. Liu, P. Čermák, C. Franz, C. Pfleiderer, and A. Schneidewind. Lattice dynamics and coupled quadrupole-phonon excitations in $CeAuAl_3$. *Phys. Rev. B*, 98:174306, 2018. .
13. D. T. Adroja, A. del Moral, C. de la Fuente, A. Fraile, E. A. Goremychkin, J. W. Taylor, A. D. Hillier, and F. Fernandez-Alonso. Vibron quasibound state in the noncentrosymmetric tetragonal heavy-fermion compound $CeCuAl_3$. *Phys. Rev. Lett.*, 108:216402, 2012.
14. S. Paschen, E. Felder, and H. R. Ott. Transp. and thermo. prop. of $CeAuAl_3$. *Eur. Phys. J. B*, 2:169–176, 1998.
15. V. Dohm and P. Fulde. Magnetoelastic interaction in rare earth systems. *Z. Phys. B*, 21:369–379, 1975.
16. E. Callen and H. B. Callen. Magnetostriction, forced magnetostriction, and anomalous thermal expansion in ferromagnets. *Phys. Rev.*, 139:A455–A471, 1965.
17. P. Fulde. Crystal fields. In *All. & Interm.*, volume 2 of *Handb. Phys. Chem. Rare Earths*, pages 295 – 386. Elsevier, 1979.
18. P. Thalmeier and B. Lüthi. The electron-phonon interaction in intermetallic compounds. In K. A. Gschneidner, editor, *Handb. Rare Earth Comp.*, volume 14 of *Handb. Phys. Chem. Rare Earths*, pages 225 – 341. Elsevier, 1991.
19. P. Morin and D. Schmitt. Quadrupolar interactions and magneto-elastic effects in rare earth intermetallic compounds. volume 5 of *Handb. Ferrom. Mat.*, pages 1 – 132. Elsevier, 1990.